2019 M_w 5.9 Mirpur, Pakistan Earthquake: Insights from Integrating Geodetic, Seismic, and Field Observations

Adnan Barkat[1,2], Farhan Javed[2], Yen Joe Tan[*1], Aamir Ali[3], Muhammad Tahir Javed[4], Nabeel Ahmad[2], Muhammad Awais[2], Muhammad Ali Shah[2], and Talat Iqbal[2]

Abstract

On 24 September 2019, an M_w 5.9 earthquake struck near the Mangla reservoir in northeastern Pakistan and resulted in 39 fatalities and 746 serious injuries, making it the deadliest earthquake in the region since the 2005 M_w 7.6 Kashmir earthquake. Here, we integrate geodetic, seismic, and field observations to characterize the source properties and impact of the Mirpur earthquake as well as investigate whether it might be a reservoir-induced event. From inverting Interferometric Synthetic Aperture Radar data, we find that a fault with strike $\sim$ 310°, dip $\sim$ 6°, and rake $\sim$ 117° is the optimal source, with slip concentrated between 5 and 6 km depth. This is consistent with our relocated aftershocks depth distribution and the lack of surface rupture observed in the field. Therefore, we infer that the earthquake ruptured the Main Himalayan Thrust (MHT). The event's shallow depth might explain the extensive damage caused despite its moderate magnitude, with a maximum shaking intensity of VIII based on our field survey. The survey also revealed extensive damages associated with earthquake-induced liquefaction. Our modeling shows that loading due to increased reservoir water level in the three months before the Mirpur earthquake led to Coulomb stress increase of $\sim$ 7–10 kPa on the rupture plane. However, this effect is $\sim$ 10 times smaller than the Coulomb stress increase due to the 2006 Mangla earthquake, and the Mirpur earthquake only occurred $\sim$ 1–2 weeks after peak water level. These suggest that pore pressure diffusion contributed to promoting the fault rupture at a time when it is close to failure due to accumulated stress from inter-seismic loading. Because the Mirpur earthquake resulted in a stress increase of > 0.2 MPa on the surrounding sections of the MHT and nearby faults, future rupture of these faults is a significant hazard and proper management of reservoir operations is necessary to prevent further elevating the seismic risk.

Introduction

The ongoing convergence of the Indian and Eurasian plates resulted in the buildup of the world's youngest and highest orogenic belt (Srivastava *et al.*, 2016). The east–west-trending Himalayan orogeny is mainly divided into four lithotectonic belts. Moving northward, these belts are separated by four mega intracontinental thrusts, namely the Main Frontal Thrust (MFT), Main Boundary Thrust, Main Central Thrust, and Main Mantle Thrust. Together, these faults are sometimes called the MFT system, with the MFT being the southernmost and youngest fault in the set. These thrust faults sole down at depth to merge with the more gently dipping detachment (Main Himalayan Thrust [MHT]), interpreted as the interface between the downgoing Indian plate and the overriding sedimentary wedge of the Himalaya (Arora *et al.*, 2012).

The MHT is the largest and one of the fastest slipping continental megathrusts on Earth, which is responsible for regional seismic productivity (e.g., 2015 M_w 7.8 Gorkha, 1950 M_w 8.5–8.7 Assam, 1934 M_w 8.4 Bihar–Nepal, 1905 M_w 7.8 Kangra earthquakes) and thus represents the primary seismic hazard in the Himalayas (Bilham *et al.*, 2017; Bilham, 2019; Dal Zilio *et al.*, 2021). Modeling of Global Positioning

1. Earth System Science Programme, Faculty of Science, The Chinese University of Hong Kong, Hong Kong, China, https://orcid.org/0000-0002-5578-3968 (AB); https://orcid.org/0000-0001-6377-7886 (YJT); 2. Centre for Earthquake Studies, National Centre for Physics, Islamabad, Pakistan, https://orcid.org/0000-0002-7168-3334 (NA); https://orcid.org/0000-0003-0758-9623 (MAS); 3. Department of Earth Sciences, Quaid-i-Azam University, Islamabad, Pakistan; 4. Department of Mathematics and Geosciences, University of Trieste, Province Trieste, Italy

*Corresponding author: yjtan@cuhk.edu.hk

1

System (GPS) measurements reveals that about 18–20 mm/yr of the convergence is accommodated by these megathrust structures in central and eastern Himalayas over ∼100 km width of the MHT (Bilham et al., 2017). In contrast, the lower convergence rate (12–14 mm/yr) and larger width (>170 km) of the MHT in western Himalaya (northern Pakistan) is still enigmatic in numerous aspects (Jouanne et al., 2020). For example, in the northern part, the occurrence of the 2005 Kashmir earthquake spotlighted the existence of significant out of sequence deformation. In the southern part, the presence of viscous décollement is inferred to permit the aseismic slip of Indian plate beneath the wide plateaus (e.g., Potwar plateau north of the Salt Range Thrust [SRT]) fronting the Kohistan mountains (Hazara Kashmir Syntaxis [HKS]) and thus, unable to sustain large earthquakes (Satyabala et al., 2012). However, previous studies have reported the occurrence of moderate magnitude earthquakes, for example, 1992 M_w 6.0 Kohat earthquake to the west and 2006 M_L 5.0 Mangla earthquake to the east of the Potwar plateau (Iqbal et al., 2009; Satyabala et al., 2012). East of the Potwar plateau (Fig. 1), no surface exposure of the MFT has been reported (Schiffman et al., 2013) and the depth and geometry of the MHT is also not well constrained. The 2006 Mangla earthquake that occurred in this region (Fig. 1) was also proposed to have ruptured a local thrust fault (Kalial Thrust [KT]) instead (Iqbal et al., 2009). Therefore, the sources of local seismicity in this region are still not well characterized. In addition, the presence of the Mangla reservoir also raises the issue of how it might affect seismic activity in the surrounding region (Brown, 1974). Improved understanding of the seismic hazard in this region is important because there is a densely populated Mirpur city nearby.

In this regard, the 24 September 2019, Mirpur earthquake (hereafter referred to as 2019 Mirpur earthquake) provides us a unique opportunity to better understand the seismic hazard of this region. This earthquake is the most damaging earthquake in northeastern Pakistan since the 2005 Kashmir earthquake. The epicenter of this event is located near the densely populated Mirpur city and the Mangla reservoir (Fig. 1). The earthquake resulted in 39 fatalities, 746 injuries and widespread damage including from earthquake-induced liquefaction reported by National Disaster Management Authority (Salman, 2019). The source parameters of this event have been reported in numerous studies (Table 1), however these were mostly based on remote observations. In this study, we constrain the source parameters and impact of this event by integrating geodetic, local seismic, and field observations and investigate its implications for seismic hazard of this region.
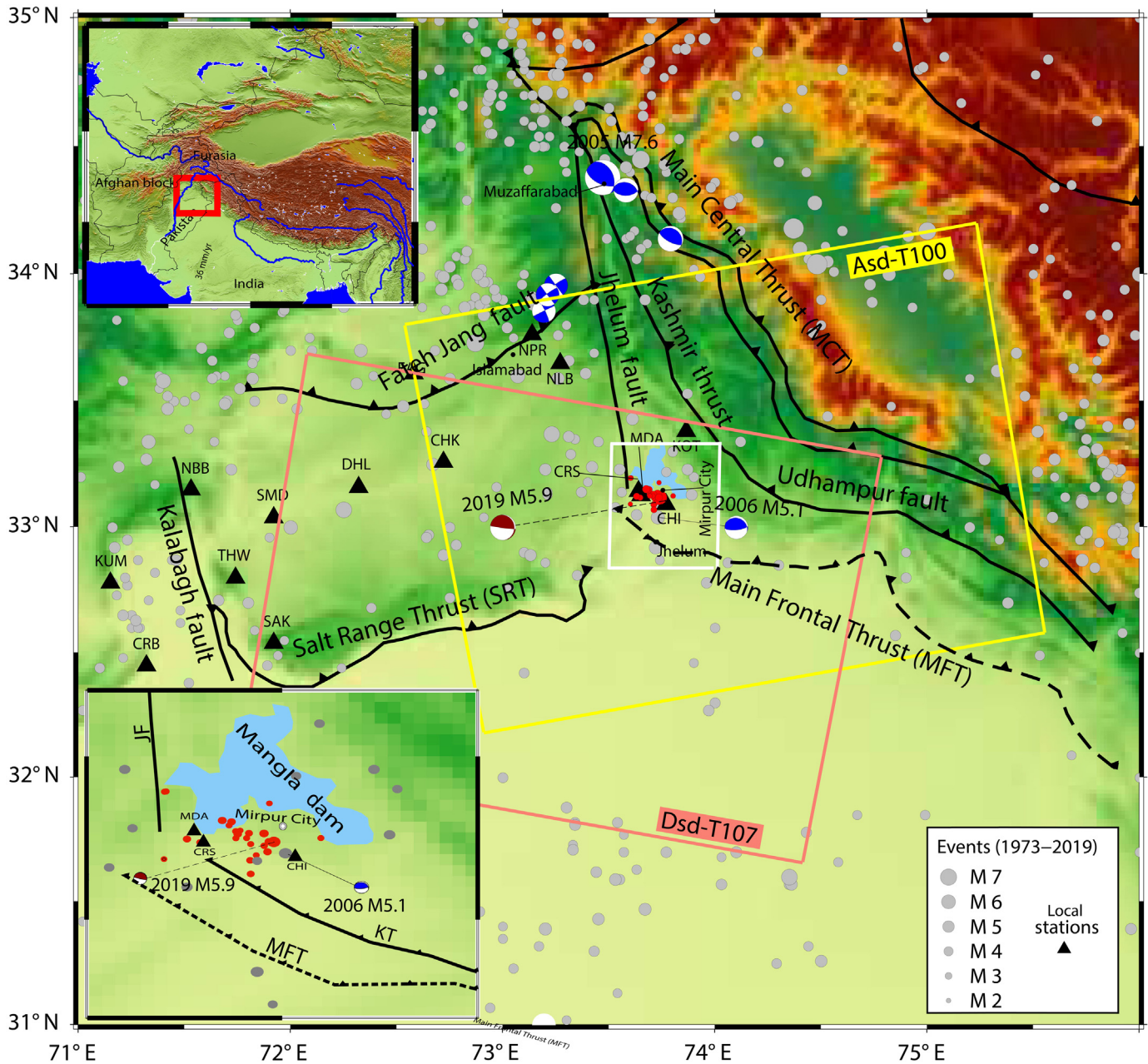
Data and Methods
The details of the methods and data utilized in this study are as follows:

Geodetic observations and slip inversion
We use Differential Interferometric Synthetic Aperture Radar to compute the coseismic deformation induced by the 2019 Mirpur earthquake. We select two pairs of Sentinel-1A observations of ascending track T-100 and descending track T-107 in Terrain Observation with Progressive Scan (TOPS) mode that have the shortest perpendicular and temporal baselines with the least seasonal atmospheric variation to retain high correlation (Table S1, available in the supplemental material to this article). We process the ascending and descending Synthetic Aperture Radar (SAR) images through GMTSAR code (Sandwell et al., 2011). In the preliminary step, we improve the coregistration through (1) geometric alignment on the basis of precise orbit (Sansosti et al., 2006), (2) deramping of single loop complex before interpolation of data (Miranda et al., 2015), and (3) mitigation of misregistration on the basis of spectral technique (Prats-Iraola et al., 2012). Azimuth coregistration is more difficult in TOPS mode acquisition than conventional strip map (De Zan and Guarnieri, 2006). After high quality coregistration, we remove the effect of topography from the SAR interferogram with the 1-arc-second Shuttle Radar Topography Mission digital elevation model (Farr and Kobrick, 2000). We use SNAPHU algorithm (Chen and Zebker, 2001) to smooth and later unwrap the interferogram. We also apply the Goldstein power filter to smooth the interferogram (Goldstein and Werner, 1998). Each subswath of interferometric SAR is processed individually and independently within their corresponding coordinates.

Interferometric Synthetic Aperture Radar (InSAR) data are known to contain spatially correlated noises that are mainly caused by phase propagation delays through the atmosphere and topographic residuals (i.e., phase change artifacts that appeared during data processing). These noises are considered as stationary and isotropic and estimated through experimental semivariogram (Fig. S1) over a mask deforming region (Knospe and Jónsson, 2010). For this purpose, the unbounded exponential one dimensional function with nugget is adopted (Sudhaus and Sigurjón, 2009). The estimated parameters of the best fitted exponential functions are presented in Table S2. Furthermore, to account for orbital and long-wavelength atmospheric delays (Sudhaus and Sigurjón, 2009), the linear ramp is estimated directly from the data during the inversion. In both steps, we estimate the errors by experimentally calculating variance and covariance matrix in each independent data set.

We adopt a two-step approach: nonlinear optimization for the best-fitting fault geometries and location assuming uniform slip, followed by nonnegative linear inversion for the slip distribution on those fault geometries. In the first step, we estimate the epicenter location, length, width, depth, strike, dip, and uniform slip of the 2019 Mirpur earthquake. To estimate the uniform slip model, a rectangular dislocation is embedded in a homogenous half-space with a shear modulus of 32 GPA

Figure 1. Topographic map of northeastern Pakistan along with the key tectonic structures labelled. The gray circles represent earthquakes from 1973 to 2019 (U.S. Geological Survey [USGS], 2021; CES catalog), with the focal mechanisms of the largest events shown as blue focal mechanisms (Global Centroid Moment Tensor [Global CMT], 2021). The red circles represent the relocated aftershocks of the 2019 Mirpur earthquake in this study. The brown focal mechanism indicates the focal mechanism of the 2019 Mirpur earthquake (Global CMT, 2021). The black triangles represent the seismic stations used in our study. The coverage of Sentinel-1A is denoted by yellow and red rectangular frames for descending and ascending tracks, respectively. The top inset shows the broader Himalayan region with our study area outlined by the red square. The bottom inset shows a zoom-in of our study area outlined by the white square. The color version of this figure is available only in the electronic edition.

and a Poisson's ratio of 0.25 (Okada, 1985). Furthermore, we subsample the interferogram into 943 and 246 points for ascending and descending datasets that increase the efficiency of the inversions (Fig. S1). More weighting is assigned to ascending data set than descending data set to minimize atmospheric delay contributions. We make sure that our subsampled data points keep the overall surface deformation shape. We then use a Bayesian inversion (GBIS) approach to invert the uniform slip model (Bagnardi and Hooper, 2018). This scientific code applies a Markov chain Monte Carlo algorithm combined with the Metropolis–Hasting algorithm to approximate the posterior probability distribution functions (PDFs) for different model parameters by evaluating a range of priori values of the source model (Mosegaard and Tarantola, 1995; Hooper *et al.*, 2013; González *et al.*, 2015). We

TABLE 1
Source Properties of the 2019 Mirpur Earthquake from Various Studies

Model	Longitude (°E)	Latitude (°N)	Depth (km)	Strike (°)	Dip (°)	Rake (°)	Length (km)	Width (km)	Slip (m)	M_w
Our preferred model (finite fault)	73.756	33.113	5.56	310	6.22	116.62	10	06	0.50	5.90
Sreejith et al. (2021) (uniform slip)	73.748	33.105	5.50	300	2.5	102	5.6	05	0.82	6.00
Xie et al. (2021) (finite fault)	73.750	33.070	4.60	277.7	4.0	79.2	07	09	0.52	5.72
Vaka et al. (2020) (uniform slip)	73.760	33.090	5.10	289.4	22.5	92.05	05	10	0.22	5.78
GFZ	73.810	33.090	10.0	249/73	8/81	86/90	-	-	-	5.30
Global CMT	73.850	32.830	14.7	246/105	10/82	52/96	-	-	-	5.70
USGS	73.790	33.080	10.0	352/98	12/87	164/78	-	-	-	5.40

GFZ, GeoForschungsZentrums; Global CMT, Global Centroid Moment Tensor; USGS, U.S. Geological Survey.

choose 1.0×10^6 iterations to compute PDFs for each source parameter and estimate optimal solution and its uncertainty.

In the second step, we perform finite slip distribution inversion by fixing strike, dip, centroid location, and reference offsets based on our best-fit uniform slip source fault models. We extend both fault length and width to 15 km to allow the inversion to constrain the extent of the slip. The fault plane is subdivided into 20 × 20 subpatches along the strike and dip of the fault, respectively. The least-square method is used to resolve the slip distribution (Jónsson et al., 2002). We also apply a smoothing operator to get more appropriate solutions (Jónsson et al., 2002). The smoothing parameter is selected according to an L-curve between roughness and root mean square (rms) misfit (Fig. S2) and ensure the coherence between individual sub-fault patches.

Seismic observations

The 2019 Mirpur earthquake was large enough to be recorded teleseismically. However, the estimated source parameters based on teleseismic data has large uncertainty for such a shallow event especially with regard to its depth (Table 1). Fortunately, the earthquake sequence was also recorded on a local seismic network maintained by the Centre for Earthquake Studies (CES) within 200 km of the epicentral region (Fig. 1). We obtain manually picked P- and S-wave arrival times from the CES for 25 events. We estimate the V_P/V_S ratio using the Wadati diagram (Wadati, 1933) by plotting the P minus S arrival times against the P arrival times of the best recorded events and obtain the V_P/V_S ratio from the slope of the best-fit line (Fig. S3a). We first locate these events using the HYPOINVERSE-2000 software (Klein, 2002) using a local P-wave velocity model provided by CES (Fig. S3b) and a

constant V_P/V_S ratio. After obtaining the initial event locations, we apply the double-difference method using the HypoDD software (Waldhauser, 2001) to obtain higher precision locations for the events (Table S3). We use pick-derived differential arrival times and apply HypoDD in the singular value decomposition mode, which allows proper estimation of location uncertainties (Waldhauser, 2001).

The Mangla Seismic Observatory (MSO) operates a seismic network near the Mangla reservoir. There are three stations within 10 km of the 2019 Mirpur sequence's epicentral region (Fig. 1). Stations within a few epicentral depths are very important for constraining the earthquake depths. We obtained event waveform data from MSO, but the stations have an unknown amount of time-varying clock drift hence the absolute arrival times could not be estimated accurately enough to be used in the earthquake location process. Nevertheless, the S minus P arrival times estimated from these waveform data could still be used to verify our obtained event locations. We align the event waveforms on the P wave arrivals and compare the predicted S-wave arrival times based on our HypoDD locations with the observed S-wave arrival times to quantify how well our obtained event locations match these near-field data.

Coulomb stress changes

We compute the Coulomb failure stress change (ΔCFS) using the Coulomb software package (Toda et al., 2011) to investigate the static stress changes on neighboring major known faults due to the 2019 Mirpur and 2006 Mangla earthquakes. We estimate ΔCFS on the Jhelum strike-slip fault as well as the MHT, MFT, and KT using receiver and source fault geometries estimated by previous studies (Iqbal et al., 2009; Jouanne et al., 2020). We use our finite slip model as the source fault for the

2019 Mirpur earthquake. The source and the receiver fault parameters used for ΔCFS computation are tabulated in Table S4. We also estimate the ΔCFS on the source faults of the 2006 Mangla and 2019 Mirpur earthquakes due to reservoir loading (Fig. S4a) using the Boussinesq solution (Liu and Zoback, 1992). We represent the Mangla reservoir by 224 point sources covering the reservoir surface and utilize the reservoir impounding history published in Xie *et al.* (2021). To estimate the ΔCFS contribution of the reservoir loading, we use a water level increase of 21 m from 349 m in July 2019 to 370 m in September 2019 (Xie *et al.*, 2021) before the 2019 Mirpur earthquake (Fig. S4b), and a water level decrease of 17 m from 357 m in November 2005 to 340 m in March 2006 before the 2006 Mangla earthquake (Fig. S4c).

Field investigations

On 25 September 2019, the day after the 2019 Mirpur earthquake, we conducted a postearthquake reconnaissance survey to assess the associated damage. This immediate field survey provides an opportunity to analyze, measure, and photographically record the effects of actual damage prior to the restoration action of local authorities and residents. The survey team visited the sites that were significantly impacted by the earthquake to (1) take photographs of damaged infrastructure along with the coordinates of the disaster-affected locations, (2) observe and document specific phenomena, for example, ground failure, lateral spreading, and liquefaction, and (3) interview eyewitnesses. We then integrate the observed ground effects, structural damage, and perceptions of local residents for intensity mapping. In total, observations are recorded at 90 locations and each site is assigned a numeric intensity value based on the European microseismic (EMS; Table S5) scale (Grunthal, 1998; Musson *et al.*, 2010). We then produce an intensity isoseismal map that covers all the meizoseismal area by interpolating between the data points.

Results

Geodetic coseismic dislocation modeling

The InSAR data reveals both positive and negative line of sight (LoS) displacements for both ascending and descending tracks (Fig. 2). Positive LoS displacement indicates the ground moved toward the satellite and negative away from the satellite. A maximum LoS displacement of around 90 mm is observed south of the Mirpur city and a minimum LoS displacement of around −70 mm is observed beneath the Mirpur city. Less atmospheric disturbance was observed in the ascending interferogram (Fig. S5a) compared to the descending interferogram (Fig. S5b). The two continuous northwest–southeast-oriented elliptical fringes (Fig. S5) is characteristic of coseismic rupture of a thrust fault striking in the northwest–southeast direction.
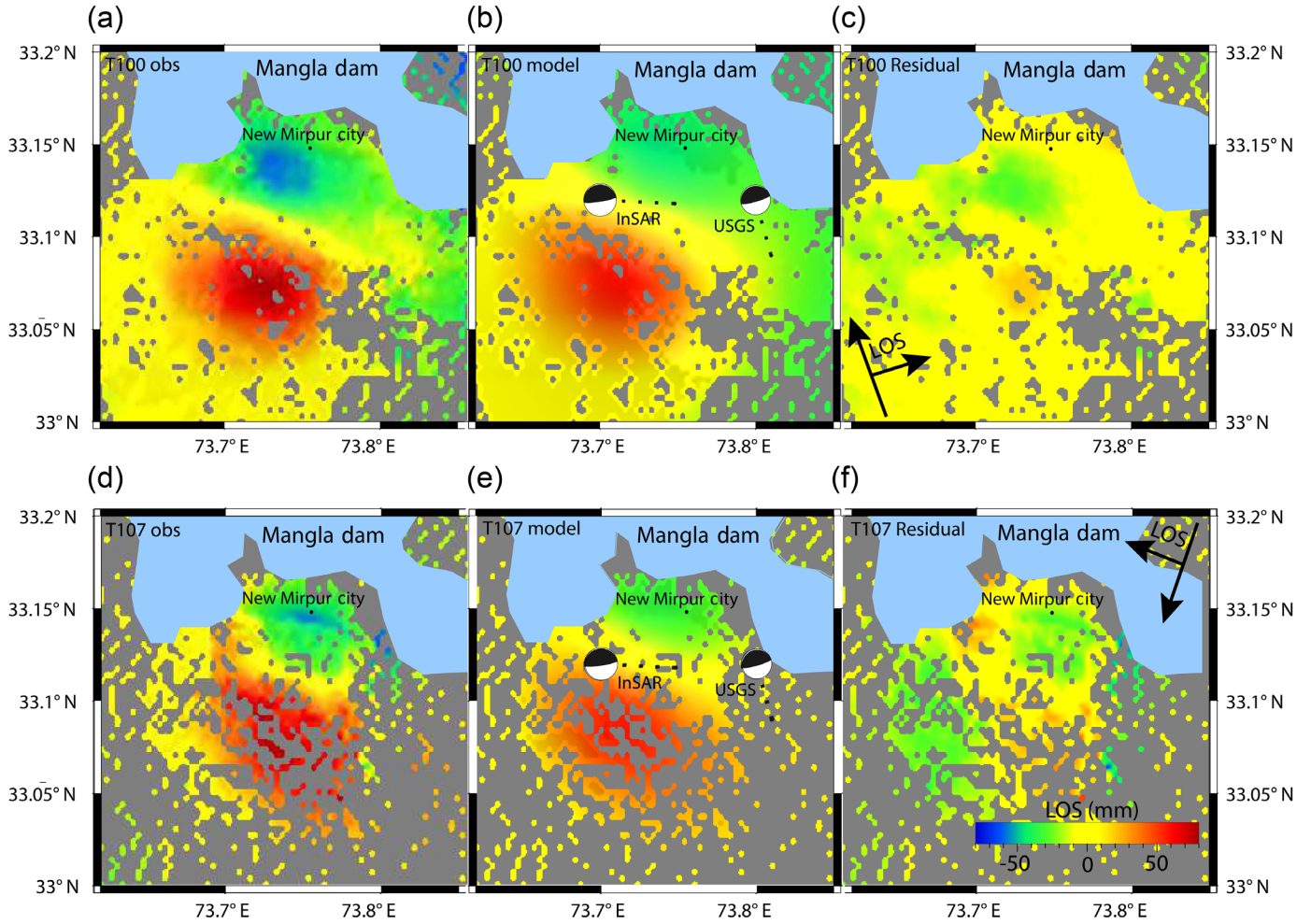
During uniform Bayesian inversion for the best-fit source parameters of the 2019 Mirpur earthquake, we set two different search intervals: a northeast, shallow-dipping (strike ∈ [200°, 350°], rake ∈ [40°, 140°], and dip ∈ [0°, 45°]) and a southwest, vertical-dipping (strike ∈ [50°, 130°], rake ∈ [40°, 140°], and dip ∈ [45°, 90°]) fault planes, based on focal mechanism solutions from previous studies (Table 1). For the northeast, shallow-dipping plane, the marginal posterior PDFs are bimodal (two peaks at strikes ∼250° and ∼320°, with rakes ∼55° and ∼120° respectively) with large uncertainty, that is, optimal values do not coincide well with the mean and median for some fault parameters such as depth, strike, rake, and dip (Fig. S6). When we narrow down the search interval for the strike to between 220° and 280° instead, the best-fit solution is ∼245° strike, ∼6° dip, and ∼52° rake (Fig. S7). However, we find that the marginal posterior PDFs are not Gaussian. This suggests that the Sentinel-1A ascending and descending data do not constrain the earthquake source parameters well, potentially due to strong atmospheric noise especially in the descending track data as well as deformation possibly due to secondary processes in the source region (Fig. 2; Fig. S5). Because the relocated aftershocks are aligned along a strike of ∼310° (Fig. 3), we also try fixing this as the fault strike and optimize for the other fault parameters. We find that in this case, the marginal posterior PDFs are Gaussian and the fault parameters are well constrained, with the best-fit solution being ∼310° strike, ∼6° dip, and ∼117° rake (Fig. S8). In contrast, the best-fit solution for the southwest, vertical-dipping plane is ∼108° strike, ∼82° dip, and ∼65° rake (Fig. S9). We subsequently use these three uniform slip inversion solutions for finite fault slip inversion.

For the northeast, shallow-dipping fault plane, the finite fault inversion results show that slip is concentrated between 5 and 6 km depth, with maximum slip of ∼0.5 m centered at ∼5.5 km depth (Fig. 4a; Fig. S2b–d). The rupture area with >0.1 m of slip is ∼144 km^2. In comparison, for the southwest, vertical-dipping fault plane, slip is more broadly distributed between 5 and 15 km depth, with maximum slip of ∼0.4 m centered at ∼8 km depth (Fig. 4b; Fig. S2c). The rupture area with > 0.1 m of slip is ∼169 km^2. The rms of the misfits between geodetic data and the model predictions are ∼0.97 cm, ∼1.1 cm, and ∼1.2 cm for the shallow dipping strike ∼310°, shallow dipping strike 250°, and vertical-dipping faults, respectively (Fig. S2a).

Seismicity relocation

Our relocation results show that the 2019 Mirpur earthquake is located at ∼6.1 km depth with the aftershocks mostly concentrated between 3.5 and 7.5 km depth (Fig. 3b; Table S3). S minus P arrival times of the mainshock and two aftershocks at the nearest stations within 10 km distance are consistent with the predicted arrival times based on our relocation results and velocity model (Fig. 3c). This suggests that the shallow depths of these events (Fig. 3b) are well constrained by near-field seismic stations. In map view, the seismicity are

Figure 2. Line-of-sight (LoS) displacement of Interferometric Synthetic Aperture Radar (InSAR) data, model and residual. (a–c) Ascending track and (d–f) descending track. (a,d) Unwrapped displacement maps; (b,e) displacement maps predicted by best-fit source model; (c,f) difference between observation and model prediction. The black focal mechanisms show the focal mechanism solutions of the 2019 Mirpur earthquake by our InSAR inversion and the USGS (2021). The color version of this figure is available only in the electronic edition.

aligned at around 310° strike (Fig. 3b), which we infer as the strike of the rupture fault plane.

Coulomb stress distribution

Assuming that the 2019 Mirpur earthquake occurred on the MHT, it resulted in a Coulomb stress increase of more than 0.2 MPa up-dip and down-dip of its rupture zone (Fig. 5a). It also resulted in a stress increase of up to 0.2 MPa on the KT and MFT (Fig. S10a). In addition, we find that the 2006 Mangla earthquake resulted in ∼0.1 MPa of stress increase on the rupture plane of the 2019 Mirpur earthquake (Fig. 5b; Fig. S10b). Finally, ΔCFS due to reservoir loading on the rupture planes of the 2019 Mirpur and 2006 Mangla earthquakes are ∼7–10 kPa (Fig. S11a) and around −5 kPa (Fig. S11b), respectively.

Field observations

The meizoseismal area of the 2019 Mirpur earthquake, which is above the rupture plane, was assigned an intensity VIII on the EMS scale (Fig. 6a; Table S5). Regions of intensity VIII experienced partial damage in reinforce concrete structures (Fig. 6b) and great damage in poorly built structures. VII intensity is assigned for regions with slight to moderate damage

(Fig. 6c). In the region of intensity VI, resident reported very strong shaking felt and partial damage of poorly constructed structures, that is, cracks in wall (Fig. 6d). Besides this, another crucial factor that increased the level of damage in the meizoseismal area is earthquake-induced liquefaction (Fig. 6a; red rectangle). Figure 6e depicts the damage caused by liquefaction in the form of ground failure and lateral spreading.

Discussions

Based on teleseismic data, there are two possible fault plane solutions for the 2019 Mirpur earthquake: southwest and northeast dipping (Table 1) (GeoForschungsZentrums [GFZ], 2021; Global Centroid Moment tensor [Global CMT], 2021;
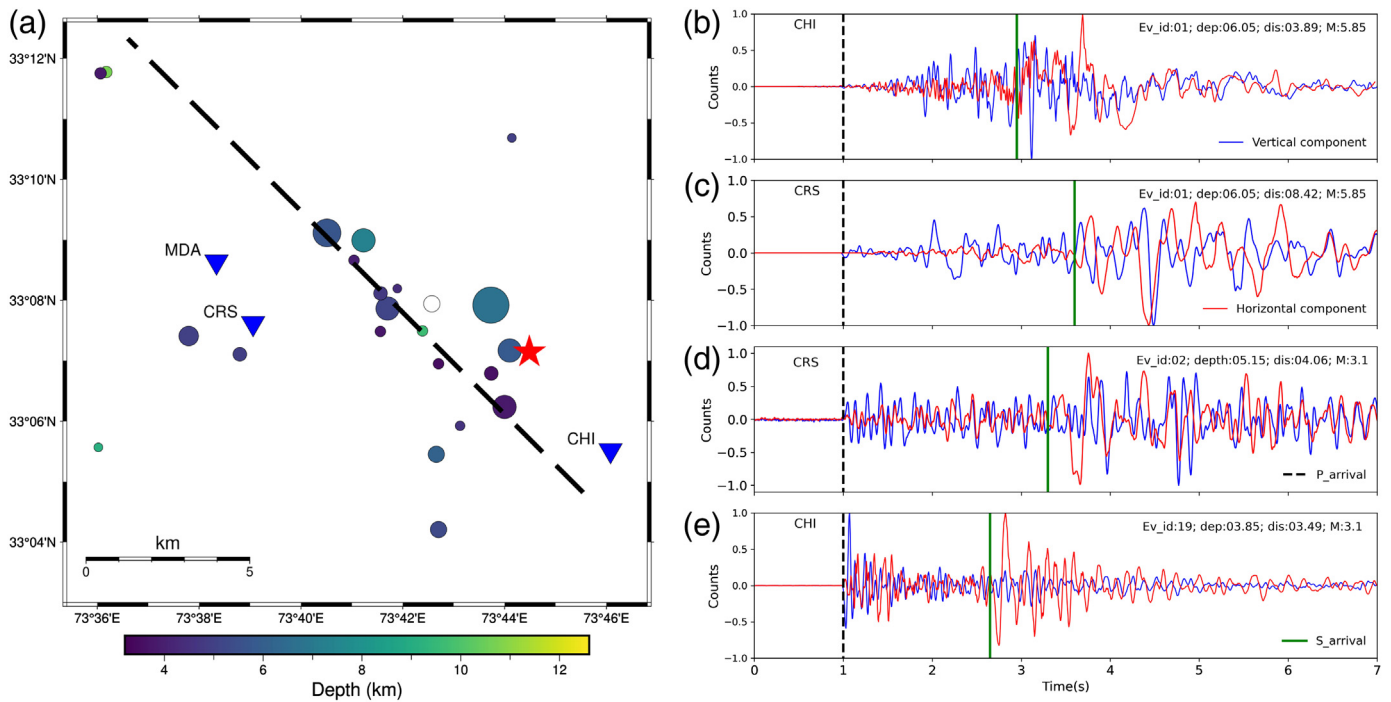
Figure 3. (a) Zoom in map of relocated aftershocks of the 2019 Mirpur earthquake (red star) in our study. Circles marking the aftershocks are color-coded by depth with marker size scaled with event magnitude (M_L 1.6–3.8). The blue triangles mark the three closest seismic stations used in our study. The dashed black line is of strike 310°. (b–e) Vertical (blue) and horizontal-component (red) seismograms of the (b,c) mainshock and (d, e) aftershocks recorded at the two nearest stations CRS and CHI. Waveforms are aligned on the P-wave arrival time (dashed black vertical line). The S-wave arrival times predicted using our relocated locations are marked by green vertical lines. The color version of this figure is available only in the electronic edition.
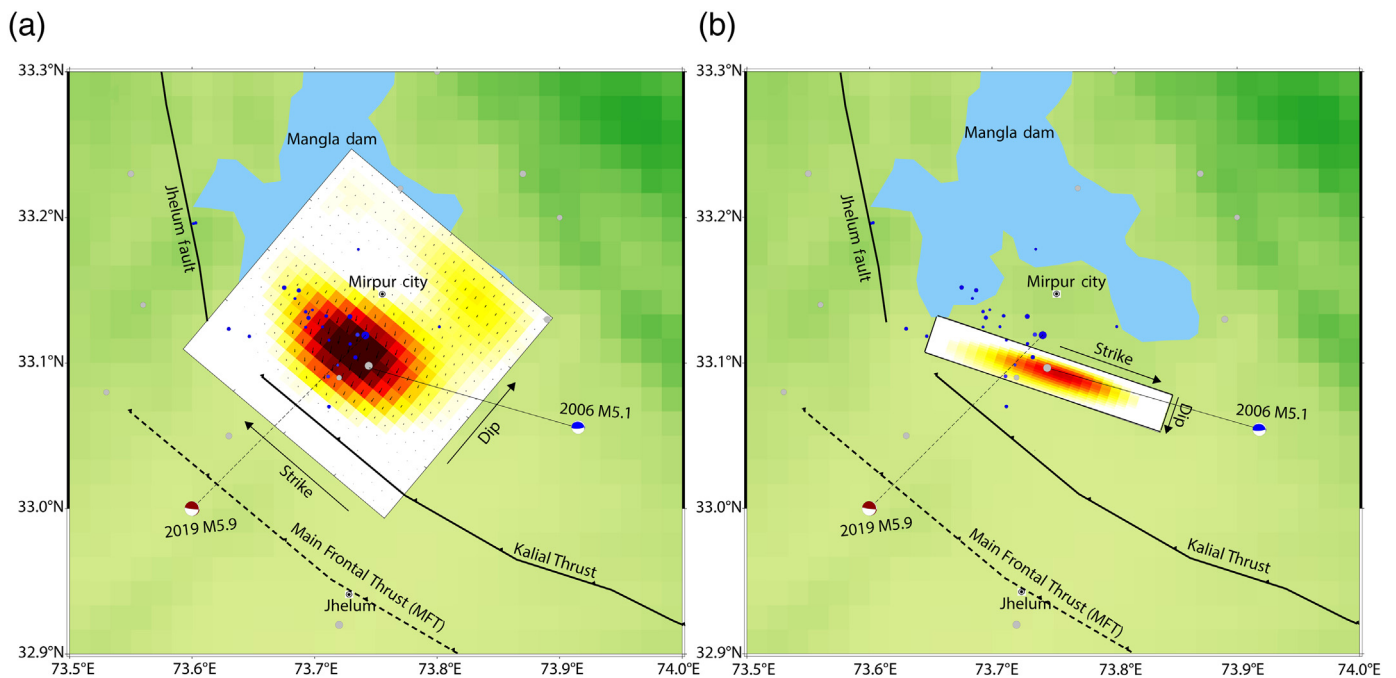
Figure 4. Finite fault slip distribution for (a) northeast-dipping (strike = 310°; dip = 6°; and rake = 117°) and (b) southwest-dipping (strike = 108°; dip = 82°; and rake = 65°) planes. The blue circles show the aftershocks relocated in our study, whereas gray circles depict historical seismicity in this region (USGS, 2021). The black solid lines mark the left lateral Jhelum strike-slip fault and Kalial local thrust fault (Iqbal et al., 2009). The black dotted line represents the inferred location of the Main Frontal Thrust (Jouanne et al., 2020). The color version of this figure is available only in the electronic edition.
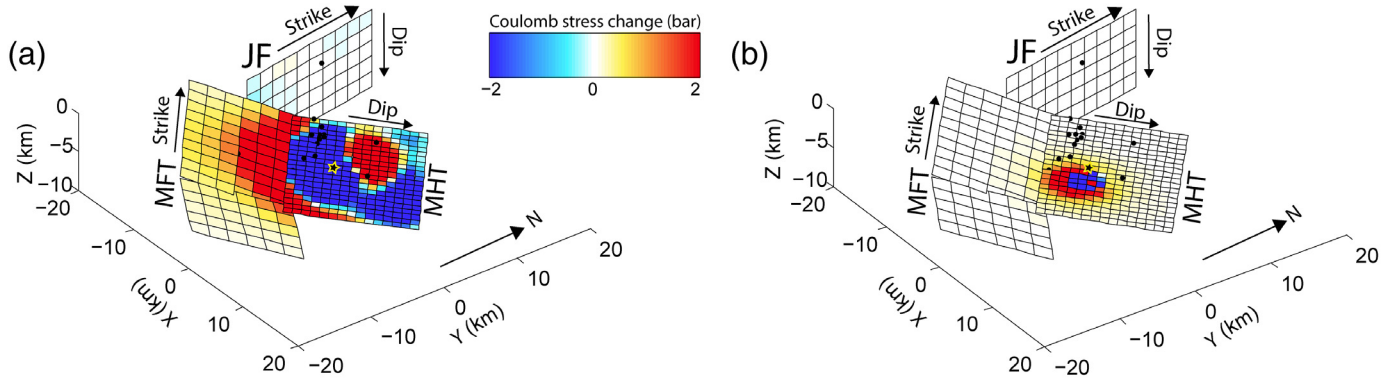
Figure 5. 3D view of estimated Coulomb failure stress change (ΔCFS) on major neighboring faults due to (a) 2019 Mirpur and (b) 2006 Mangla earthquakes. The black circles mark the relocated aftershocks of the 2019 Mirpur earthquake (black star). The color version of this figure is available only in the electronic edition.
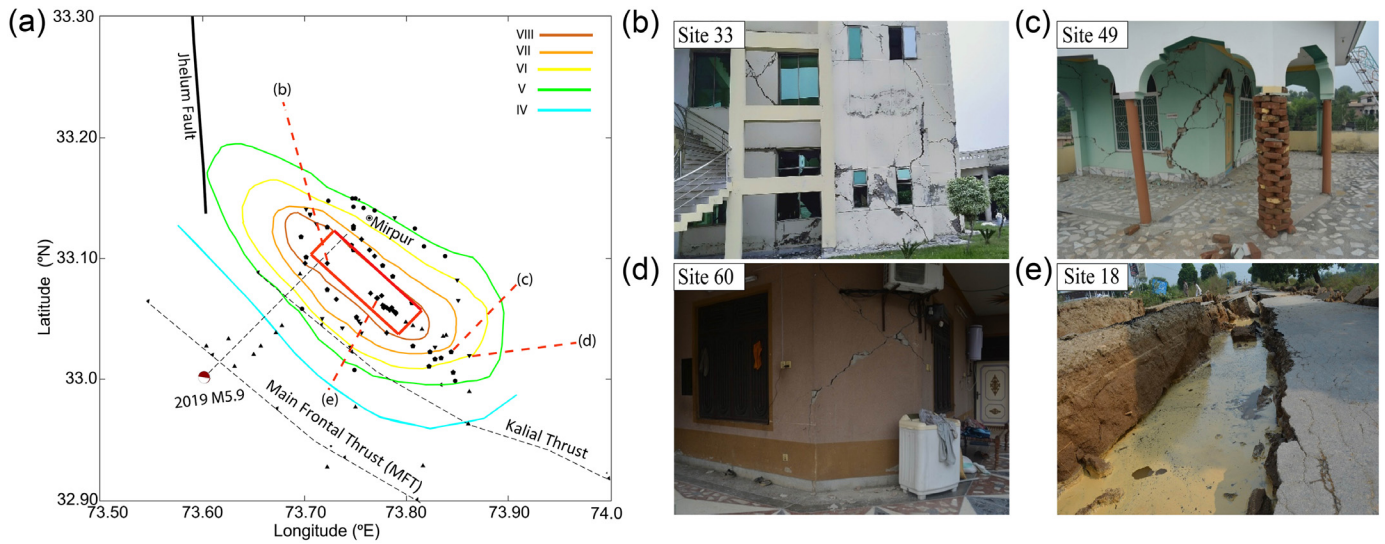

Figure 6. (a) European macroseismic (EMS) intensity observations are denoted by black symbols: VIII by square, VII by polygon, VI by down pointing triangle, V by circle, and IV by up-pointing triangle. Colored contours show the intensity isoseismal lines. It should be noted that during the survey, some areas were not accessible due to high relief and waterbody. In sparsely populated areas without manmade structures, intensity values were assessed based on environmental features such as ground fractures, rock fall, and slop failures (locations of the sites are listed in Table S5). Earthquake-induced liquefaction is mainly observed within the region bounded by red rectangle. (b–e) Pictures of damage and liquefaction recorded at various observational points (marked in panel a) taken by the survey team on 25 September 2019, one day after the 2019 Mirpur earthquake. (b) Damage to well-designed structures at site number 33 and marked as intensity level VIII. (c) Moderate damage to infrastructure observed at site number 49 and marked as intensity level VII. (d) Slight damage to poorly designed structure with strong shaking felt by residents at site number 60 and marked as intensity level VI. (e) Liquefaction observed at site number 18. The color version of this figure is available only in the electronic edition.

U.S. Geological Survey [USGS], 2021). However, by considering the prevailing thrust tectonic background in northwest Himalayan foreland, the high-angle, southwest-dipping thrust event is unlikely (Jouanne *et al.*, 2020). Therefore, previous studies based on InSAR deformation modeling only searched within the parameter ranges of a northeast-dipping fault plane (Vaka *et al.*, 2020; Sreejith *et al.* 2021; Xie *et al.*, 2021). Vaka *et al.*

(2020) proposed a northeast-dipping (∼22.5°) splay fault (MFT) of MHT as an optimal source of the 2019 Mirpur earthquake. In contrast, Sreejith *et al.* (2021) and Xie *et al.* (2021) best-fit model is a shallow dipping (∼2.5°–4.0°) source and inferred that the MHT is the source fault. By considering both southwest and northeast-dipping planes, our best-fit single-fault model from InSAR modeling is a northeast-dipping

source with strike ∼310°, dip ∼6°, and rake ∼117° (Table 1 and Table S6).

However, considering the findings of Vaka *et al.* (2020), there is a possibility that the 2019 Mirpur earthquake ruptured both the MHT and MFT, similar to what was proposed for the Kishtwar earthquake (May 2013 M_b 5.7 event ∼180 km northeast of the 2019 Mirpur earthquake; Mitra *et al.*, 2014). To explore this possibility, we perform a finite slip inversion assuming a two fault model, allowing slip on both a 6°-dipping (MHT) and a 20°-dipping (MFT) fault (Fig. S12). We then evaluate this model relative to our single fault models using the Akaike Information Criterion (AIC) to investigate whether the increase in model complexity significantly improves the data fit (Akaike, 1985). We find that the single-fault model has the lowest AIC value (Table S7), hence a two-fault model is not warranted. Therefore, we conclude that the 2019 Mirpur earthquake ruptured a single, northeast-dipping fault (dip ∼6°) that is likely the MHT.

In addition to the source fault geometry, the magnitude and depth of the 2019 Mirpur earthquake from previous studies also show considerable variation (Table 1). Based on teleseismic observations, the 2019 Mirpur earthquake is a moderate magnitude (M_w 5.3–5.7) event seated at a depth of ∼10–14.7 km (Table 1; GFZ, 2021; Global CMT, 2021; USGS, 2021). In comparison, studies based on InSAR-based deformation modelling found a relatively shallow (4.6–5.5 km) and larger magnitude (M_w 5.5–6) source (Vaka *et al.*, 2020; Sreejith *et al.*, 2021; Xie *et al.*, 2021). Our InSAR-based uniform-slip model shows that the 2019 Mirpur earthquake has $M_w \sim 5.9$ and is seated at a depth of ∼5.6 km (Table 1), similar to the depth of ∼6.1 km obtained from our relocation using the local seismic data. Furthermore, our preferred finite fault inversion model shows that coseismic slip (>0.1 m) is distributed from 5 to 6 km depth, which coincide with our relocated aftershocks depth range of 3.5–7.5 km. The coseismic slip not reaching the surface agrees well with the lack of surface rupture observed during our field survey. Collectively, based on the seismic, field, and InSAR observations, we propose the optimal depth of this event is ∼6 km. The greater depths reported by teleseismic studies (GFZ, 2021; Global CMT, 2021; USGS, 2021) is likely due to their lack of depth constraints for such a shallow event. In addition, the larger magnitude reported by our study as well as other InSAR-based studies (Vaka *et al.*, 2020; Sreejith *et al.*, 2021; Xie *et al.*, 2021) compared to the teleseismic reports (Table 1) could be due to postseismic processes in the source region, though further study is necessary to verify this hypothesis.

In comparison with the 2019 Mirpur earthquake, the 2006 Mangla earthquake was proposed to have occurred on a northeast, gently dipping fault (Table 1; Table S8). Both USGS and Global CMT have similar solutions for the 2006 Mangla earthquake of strike 246°, dip 21°, and rake 61°, but differ in depth. USGS proposed a relatively shallow source at ∼10 km depth, whereas Global CMT proposed a deeper source at 24.7 km depth

(Table S8). Iqbal *et al.* (2009) proposed similar source parameters (strike ∼293°, dip ∼20°, rake ∼117°, and depth ∼10 km) as USGS using local arrival time and *P*-wave polarity data. The strain accumulation (at maximum ∼11 mm/yr; Schiffman *et al.*, 2013) over the 13 yr period would be ∼14 cm, which is significantly smaller than the average slip (∼50 cm) of the 2019 Mirpur earthquake. Therefore, the 2019 Mirpur and 2006 Mangla earthquakes likely did not rupture the same asperity. Considering the 20°-dipping fault plane solution for the 2006 Mangla earthquake and its epicentral location further south, it likely occurred on a different fault, for example, KT or MFT (Fig. 4).

The nature (locking or creeping) and depth of the décollement in the region east of the Potwar plateau where the 2019 Mirpur earthquake occurred is not well constrained. Nevertheless, studies in the surrounding regions (Satyabala *et al.*, 2012; Vassallo *et al.*, 2015; Sharma *et al.*, 2018; Priestley *et al.*, 2019; Jouanne *et al.*, 2020) can provide some guidance. For instance, based on *P*-wave receiver function analysis, Sharma *et al.* (2018) and Priestley *et al.* (2019) reported that the MHT beneath the sub-Himalayan (stations distributed to the west and north of our study region) dips toward the northeast at ∼7° and is located a depth of 8–10 km. This is consistent with our interpretation that the 2019 Mirpur earthquake occurred on the MHT. West of the Potwar plateau, Satyabala *et al.* (2012) proposed the existence of a viscous layer of Eo-Cambrian salt hence the décollement mostly accommodates strain aseismically with only moderate magnitude earthquakes, for example, the 1992 M_w 6.0 Kohat earthquake, occurring on isolated asperities. Some of these viscous materials might have been evacuated to the surrounding décollement (Satyabala *et al.*, 2012), which could explain the lack of historical $M_w > 6$ earthquakes in the Mirpur region. If this is indeed the case, the 2019 Mirpur earthquake might have ruptured an isolated asperity within a region of the MHT. Although, Jouanne *et al.* (2020) found that this section of the MHT is strongly coupled based on modeling GPS observations, this result is not well constrained due to limited station coverage as reflected by the large residual misfit (Jouanne *et al.* 2020 fig. 10). Regardless, since the 2019 Mirpur earthquake resulted in >0.2 MPa of stress increase up-dip and down-dip of its rupture zone, future rupture of this section of the MHT is likely a significant hazard for this region. Our result is consistent with Sreejith *et al.* (2021) which also reported stress increase on the up-dip portion of the MHT. We find that the 2019 Mirpur earthquake resulted in ∼0.1 MPa of stress increase on both the MFT and the KT, where the 2006 Mangla earthquake occurred. Sreejith *et al.* (2021) also reported an increase in coseismic Coulomb stress of >0.05 MPa on the MFT and the frontal anticline system. Therefore, rupture of these faults is also a significant future hazard.

Considering both the 2006 Mangla and 2019 Mirpur earthquakes occurred near the Mangla reservoir, it is worthwhile to explore whether they are reservoir-induced events. Xie *et al.* (2021) found that the direct loading effect due to an increase

of reservoir storage by ~4.5 km^3 in the three months before the 2019 Mirpur earthquake resulted in a Coulomb stress increase of ~7 kPa at the maximum coseismic rupture zone. The Coulomb stress increase can be further amplified to 15–25 kPa when incorporating pore pressure effect depending on the assumed hydraulic diffusivity (Xie et al., 2021). Because the amplitude of stress increase is comparable to previous studies of reservoir-induced earthquakes (Gahalaut and Hassoup, 2012; Tuan et al., 2017; Gahalaut et al., 2018), they inferred that the surge in reservoir loading promoted the occurrence of the 2019 Mirpur earthquake. Our calculation of ΔCFS shows a stress increase of 5–10 kPa (Fig. S11a) due to reservoir loading on our preferred fault model of the 2019 Mirpur earthquake which is consistent with Xie et al. (2021). However, we note that the 2019 Mirpur earthquake occurred ~1–2 weeks after peak water level during a period of water release (Fig. S4b). Similarly, the 2006 Mangla earthquake followed a decrease in reservoir level by ~30 m when a Coulomb stress decrease of ~5 kPa (Figs. S4c, S11b) due to the direct unloading effect should have inhibited its occurrence. This points to the importance of water diffusion from the reservoir to the fault zone in controlling reservoir-induced seismicity, where peak pore pressure lags peak water level and the fault is most destabilized sometime after peak water level (Roeloffs, 1988; Simpson et al., 1988). We find that the 2006 Mangla earthquake in turn resulted in a Coulomb stress increase of ~100 kPa on the eventual rupture zone of the 2019 Mirpur earthquake (Fig. 5b). This is ~10 times larger than the estimated stress increase due to reservoir loading and pore pressure diffusion in 2019 (Xie et al., 2021). In addition, episodic upsurges in reservoir water level during 2013–2017 that are of similar magnitude to that in 2019 (Xie et al., 2021) did not correlate with notable increase in earthquake activity nearby (Fig. S4a), similar to the lack of significant change in background seismicity during the initial filling period of the Mangla reservoir (Adams and Ahmed, 1969). These suggest that the smaller stress increase from reservoir loading and pore pressure diffusion was only able to trigger the 2019 Mirpur earthquake because the fault is closer to failure due to accumulated stress from inter-seismic loading, consistent with the estimated coseismic stress drop (Sreejith et al., 2021) being much larger than the estimated Coulomb stress change.

The intensity pattern of the 2019 Mirpur earthquake is aligned along the source strike (northwest–southeast-trending) with the highest intensity (EMS-VIII) above the inferred rupture plane (Fig. 6a). In comparison, the USGS's model prediction shows a relatively concentric intensity pattern with a lower maximum intensity of modified Mercalli intensity VII around the epicentral region (Fig. S13). This is likely due to the point source of deeper depth (Table 1) used in USGS's model and potential underestimation of local site amplification effect due to the presence of unconsolidated sedimentary strata in this region (Bhadran et al., 2022; Gardezi et al., 2021). USGS's model similarly underestimated the shaking intensity for the 2006 Mangla

earthquake compared to field observations reported by Iqbal et al. (2009). In addition, we only observed liquefaction in the highest intensity region of the 2019 Mirpur earthquake (Fig. 6a) whereas USGS's model predicted high liquefaction potential in far-field regions (Fig. S13). This discrepancy could be due to smaller scale heterogeneity in site conditions unaccounted for in USGS's model. Our results demonstrate the importance of incorporating higher resolution regional data to improve model estimates of earthquake impacts for disaster planning.

Conclusions

The integration of geodetic, seismic, and field observations shows that the 2019 Mirpur earthquake ruptured the northeast-shallow-dipping MHT at ~6 km depth, unlike the 2006 Mangla earthquake which ruptured a more steeply dipping local thrust fault. Despite its moderate magnitude, the 2019 Mirpur earthquake caused widespread damage due to its shallow depth and local site amplification effects which contributed to large shaking intensity. Damages were further amplified by earthquake-induced liquefaction. In addition to reservoir loading, pore pressure diffusion also contributed to promoting the occurrence of the 2019 Mirpur earthquake at a time when the fault is close to failure due to accumulated stress from inter-seismic loading and the stress increase caused by the nearby 2006 Mangla earthquake. Because the 2019 Mirpur earthquake resulted in significant stress increases on the MHT and surrounding faults, rupture of these faults is likely a significant future hazard. Therefore, proper management of the Mangla reservoir's operations is necessary to prevent further elevating the earthquake risk in this region.

Data and Resources

The initial earthquake catalog and arrival time picks were provided by Centre for Earthquake Studies. The seismic waveforms were provided by the Mangla Seismic Observatory (Water and Power Development Authority, Pakistan). The catalog of regional seismicity plotted in Figure 1 was downloaded from U.S. Geological Survey (USGS; https://earthquake.usgs.gov/earthquakes/search/). Focal mechanisms were downloaded from Global Centroid Moment tensor (Global CMT; https://ds.iris.edu/spud/momenttensor). The hypoDD (https://www.usgs.gov/software/hypodd), Hypoinverse v1.4 (https://www.usgs.gov/software/hypoinverse-earthquake-location) and Coulomb 3; https://www.usgs.gov/software/coulomb-3) software packages are publicly available. The Generic Mapping Tool 6.0 (https://www.generic-mapping-tools.org/) was used to prepare some figures. Sentinel-1 data are available through Copernicus Open Access Hub website (https://scihub.copernicus.eu/dhus/#/home). The supplemental material includes 13 figures and 8 tables, providing additional information on data and modeling results. All websites were last accessed in September 2021.

Declaration of Competing Interests

The authors acknowledge that there are no conflicts of interest recorded.

Acknowledgments

References

Adams, R. D., and A. Ahmed (1969). Seismic effects at Mangla dam, Pakistan, *Nature* **222,** 1153–1155, doi: 10.1038/2221153a0.

Akaike, H. (1985). Prediction and entropy, in *Selected Papers of Hirotugu Akaike*, Springer, New York, New York, U.S.A., 387–410.

Arora, B. R., V. K. Gahalaut, and N. Kumar (2012). Structural control on along-strike variation in the seismicity of the northwest Himalaya, *J. Asian Earth Sci.* **57,** 15–24, doi: 10.1016/j.jseaes.2012.06.001.

Bagnardi, M., and A. Hooper (2018). Inversion of surface deformation data for rapid estimates of source parameters and uncertainties: A Bayesian approach, *Geochem. Geophys. Geosys.* **19,** no. 7, 2194–2211, doi: 10.1029/2018GC007585.

Bhadran, A., K. M. Sreejith, D. Girishbai, B. P. Duarah, R. Agrawal, and G. Gopinath (2022). An appraisal of ground failure and hydrogeological changes associated with the 28 April 2021 Mw 6 Sonitpur earthquake, Assam, India, using field evidence and InSAR measurements, *Seismol. Res. Lett.* doi: 10.1785/0220210257.

Bilham, R. (2019). Himalayan earthquakes: A review of historical seismicity and early 21st century slip potential, *Geol. Soc. Lond. Spec. Publ.* **483,** 423–482, doi: 10.1144/SP483.16.

Bilham, R., D. Mencin, R. Bendick, and R. Bürgmann (2017). Implications for elastic energy storage in the Himalaya from the Gorkha 2015 earthquake and other incomplete ruptures of the main Himalayan thrust, *Quat. Int.* **462,** 3–21, doi: 10.1016/j.quaint.2016.09.055.

Brown, R. L. (1974). Seismic activity following impounding of Mangla reservoir, *Eng. Geol.* **8,** nos. 1/2, 79–93, doi: 10.1016/0013-7952(74)90014-3.

Chen, C. W., and H. A. Zebker (2001). Two-dimensional phase unwrapping with use of statistical models for cost functions in nonlinear optimization, *J. Opt. Soc. Am. A* **18,** no. 2, 338–351, doi: 10.1364/JOSAA.18.000338.

Dal Zilio, L., G. Hetényi, J. Hubbard, and L. Bollinger (2021). Building the Himalaya from tectonic to earthquake scales, *Nat. Rev. Earth Environ.* **2,** no. 4, 251–268, doi: 10.1038/s43017-021-00143-1.

De Zan, F., and A. M. Guarnieri (2006). TOPSAR: Terrain observation by progressive scans, *IEEE Trans. Geosci. Remote Sens.* **44,** no. 9, 2352–2360, doi: 10.1109/TGRS.2006.873853.

Farr, T. G., and M. Kobrick (2000). Shuttle radar topography mission produces a wealth of data, *Eos Trans. AGU* **81,** no. 48, doi: 10.1029/EO081i048p00583.

Gahalaut, K., and A. Hassoup (2012). Role of fluids in the earthquake occurrence around Aswan reservoir, Egypt, *J. Geophys. Res.* **117,** no. B2, doi: 10.1029/2011JB008796.

Gahalaut, K., S. Gupta, V. K. Gahalaut, and P. Mahesh (2018). Influence of Tehri reservoir impoundment on local seismicity of northwest Himalaya, *Bull. Seismol. Soc. Am.* **108,** no. 5B, 3119–3125, doi: 10.1785/0120180077.

Gardezi, S. A. H., G. Hussain, B. Neupane, M. Imran, Q. Y. Hamid, N. Ikram, and H. Asghar (2021). Geological investigation of 5.6 MW Mirpur earthquake, northwestern Himalayas, Pakistan, *Int. J. Earth Sci.* **9,** no. 01, 20–31.

German Research Centre for Geosciences (GFZ) (2021). GEOFON program, available at https://geofon.gfz-potsdam.de/eqinfo/list.php (last accessed September 2021).

Global Centroid Moment Tensor Catalog (Global CMT) (2021). Available at https://www.globalcmt.org/CMTsearch.html (last accessed September 2021).

Goldstein, R. M., and C. L. Werner (1998). Radar interferogram filtering for geophysical applications, *Geophys. Res. Let.* **25,** no. 21, 4035–4038, doi: 10.1029/1998GL900033.

González, P. J., M. Bagnardi, A. J. Hooper, Y. Larsen, P. Marinkovic, S. V. Samsonov, and T. J. Wright (2015). The 2014–2015 eruption of Fogo volcano: Geodetic modeling of Sentinel-1 TOPS interferometry, *Geophys. Res. Lett.* **42,** no. 21, 9239–9246, doi: 10.1002/2015GL066003.

Grunthal, G. (1998). European Macroseismic Scale 1998 (EMS-98), in *Cahiers du Centre Européen de Géodynamique et de Séismologie*, Vol. 15, European Seismological Commission, Luxembourg (in French).

Hooper, A., J. Pietrzak, W. Simons, H. Cui, R. Riva, M. Naeije, and A. Socquet (2013). Importance of horizontal seafloor motion on tsunami height for the 2011 Mw= 9.0 Tohoku-Oki earthquake, *Earth. Planet. Sci. Lett.* **361,** 469–479, doi: 10.1016/j.epsl.2012.11.013.

Iqbal, T., K. Khan, M. Qaisar, T. Mahmood, and N. Ahmad (2009). Mangla earthquake of March 10, 2006: Source parameters and nature of the derived fault, *Geol. Bull. Punjab. Univ.* **44,** 117–122.

Jónsson, S., H. Zebker, P. Segall, and F. Amelung (2002). Fault slip distribution of the 1999 Mw 7.1 Hector Mine, California, earthquake, estimated from satellite radar and GPS measurements, *Bull. Seismol. Soc. Am.* **92,** no. 4, 1377–1389, doi: 10.1785/0120000922.

Jouanne, F., N. Munawar, J. L. Mugnier, A. Ahmed, A. A. Awan, P. Bascou, and R. Vassallo (2020). Seismic coupling quantified on inferred décollements beneath the western syntaxis of the Himalaya, *Tectonics* **39,** no. 9, e2020TC006122, doi: 10.1029/2020TC006122.

Klein, F. W. (2002). User's guide to HYPOINVERSE-2000, a Fortran program to solve for earthquake locations and magnitudes, *U.S. Geol. Surv.* doi: 10.3133/ofr02171.

Knospe, S. H. G., and S. Jónsson (2010). Covariance estimation for dInSAR surface deformation measurements in the presence of anisotropic atmospheric noise, *IEEE Trans. Geosci. Remote Sens.* **48,** no. 4, 2057–2065, doi: 10.1109/TGRS.2009.2033937.

Liu, L., and M. D. Zoback (1992). The effect of topography on the state of stress in the crust: application to the site of the Cajon pass scientific drilling project, *J. Geophys. Res.* **97,** no. B4, 5095–5108, doi: 10.1029/91JB01355.

Miranda, N., P. J. Meadows, D. Type, and T. Note (2015). Radiometric calibration of S-1 Level-1 products generated by the 1IPF, available at https://sentinel.esa.int/documents/247904/685163/S1-Radiometric-Calibration-V1.0.pdf (last accessed September 2021).

Mitra, S., S. Wanchoo, and K. F. Priestley (2014). Source parameters of the 1 May 2013 mb 5.7 Kishtwar earthquake: Implications for seismic hazards, *Bull. Seismol. Soc. Am.* **104,** no. 2, 1013–1019, doi: 10.1785/0120130216.

Mosegaard, K., and A. Tarantola (1995). Monte Carlo sampling of solutions to inverse problems, *J. Geophys. Res.* **100,** no. B7, 12,431–12,447, doi: 10.1029/94JB03097.

Musson, R. M., G. Grünthal, and M. Stucchi (2010). The comparison of macro-seismic intensity scales, *J. Seismol.* **14,** no. 2, 413–428, doi: 10.1007/s10950-009-9172-0.

Okada, Y. (1985). Surface deformation due to shear and tensile faults in a half-space, *Bull. Seismol. Soc. Am.* **75,** no. 4, 1135–1154, doi: 10.1785/BSSA0750041135.

Prats-Iraola, P., R. Scheiber, L. Marotti, S. Wollstadt, and A. Reigber (2012). TOPS interferometry with TerraSAR-X, *IEEE Trans. Geosci. Remote. Sens.* **50,** no. 8, 3179–3188, doi: 10.1109/TGRS.2011.2178247.

Priestley, K., T. Ho, and S. Mitra (2019). The crustal structure of the Himalaya: A synthesis, *Geol. Soc. Lond. Spec. Publ.* **483,** no. 1, 483–516, doi: 10.1144/SP483-2018-127.

Roeloffs, E. A. (1988). Fault stability changes induced beneath a reservoir with cyclic variations in water level, *J. Geophys. Res.* **93,** no. B3, 2107–2124, doi: 10.1029/JB093iB03p02107.

Salman, M. (2019). NMA Situation report No.11—Mirpur earthquake 2019, National Disaster Management of Authority, Islamabad.

Sandwell, D., R. Mellors, X. Tong, M. Wei, and P. Wessel (2011). GMTSAR: An InSAR processing system based on generic mapping tools, available at https://escholarship.org/uc/item/8zq2c02m (last accessed September 2021).

Sansosti, E., P. Berardino, M. Manunta, F. Serafino, and G. Fornaro (2006). Geometrical SAR image registration, *IEEE Trans. Geosci. Remote Sens.* **44,** no. 10, 2861–2870.

Satyabala, S. P., Z. Yang, and R. Bilham (2012). Stick–slip advance of the Kohat plateau in Pakistan, *Nat. Geosci.* **5,** no. 2, 147–150, doi: 10.1038/ngeo1373.

Schiffman, C., B. S. Bali, W. Szeliga, and R. Bilham (2013). Seismic slip deficit in the Kashmir Himalaya from GPS observations, *Geophys. Res. Lett.* **40,** no. 21, 5642–5645, doi: 10.1002/2013GL057700.

Sharma, S., D. Powali, S. Mitra, S. K. Wanchoo, K. Priestley, and V. Gaur (2018). Lithospheric structure and earthquakes beneath Jammu and Kashmir Himalaya, *EGU General Assembly Conference Abstracts*.

Simpson, D. W., W. S. Leith, and C. H. Scholz (1988). Two types of reservoir-induced seismicity, *Bull. Seismol. Soc. Am.* **78,** no. 6, 2025–2040, doi: 10.1785/BSSA0780062025.

Sreejith, K. M., M. C. M. Jasir, R. Agrawal, and A. S. Rajawat (2021). The 2019 September 24, Mw= 6, Mirpur earthquake, NW Himalaya: Geodetic evidence for shallow, near-horizontal décollement rupture of the main Himalayan thrust, *Tectonophysics* **816,** doi: 10.1016/j.tecto.2021.229013.

Srivastava, V., M. Mukul, and J. B. Barnes (2016). Main frontal thrust deformation and topographic growth of the Mohand range, northwest Himalaya, *J. Struct. Geol.* **93,** 131–148, doi: 10.1016/j.jsg.2016.10.009.

Sudhaus, H., and J. Sigurjón (2009). Improved source modelling through combined use of InSAR and GPS under consideration of correlated data errors: Application to the June 2000 Kleifarvatn earthquake, Iceland, *Geophys. J. Int.* **176,** no. 2, 389–404, doi: 10.1111/j.1365-246X.2008.03989.x.

Toda, S., R. S. Stein, V. Sevilgen, and J. Lin (2011). Coulomb 3.3 Graphic-rich deformation and stress-change software for earthquake, tectonic, and volcano research and teaching—User guide, *U.S. Geol. Surv. Open-File Rept. 2011-1060*, available at https://pubs.usgs.gov/of/2011/1060/.

Tuan, T. A., N. P. Rao, K. Gahalaut, C. D. Trong, C. Chien, and K. Mallika (2017). Evidence that earthquakes have been triggered by reservoir in the Song Tranh 2 region, Vietnam, *J. Seismol.* **21,** no. 5, 1131–1143, doi: 10.1007/s10950-017-9656-2.

U.S. Geological Survey (USGS) (2021). Earthquake catalog, available at https://earthquake.usgs.gov/earthquakes/search/ (last accessed September 2021).

Vaka, D. S., Y. S. Rao, and T. Singh (2020). Surface deformation of the 2019 Mirpur earthquake estimated from Sentinel-1 InSAR data, *2020 IEEE India Geoscience and Remote Sensing Symposium (InGARSS)*, IEEE, doi: 10.1109/InGARSS48198.2020.9358915.

Vassallo, R., J. L. Mugnier, V. Vignon, M. A. Malik, R. Jayangondaperumal, P. Srivastava, and J. Carcaillet (2015). Distribution of the late-Quaternary deformation in northwestern Himalaya, *Earth Planet. Sci. Lett.* **411,** 241–252, doi: 10.1016/j.epsl.2014.11.030.

Wadati, K. (1933). On the travel time of earthquake waves. Part. II. *Geophys. Mag.* **7,** 101–111.

Waldhauser, F. (2001). hypoDD—A program to compute double-difference hypocenter locations, doi: 10.7916/D8SN072H.

Xie, L., W. Xu, X. Liu, and X. Ding (2021). Surge of Mangla reservoir loading promoted failure on active décollement of western Himalayas, *Int. J. Appl. Earth Obs. Geoinf.* **102,** doi: 10.1016/j.jag.2021.102401.